Computational optimization of adhesive microstructures based on a nonlinear beam formulation

Janine C. Mergel[a], Roger A. Sauer[1,a] and Anupam Saxena[b]

[a] *Graduate School AICES, RWTH Aachen University, Templergraben 55, 52056 Aachen, Germany*
[b] *Department of Mechanical Engineering, IIT Kanpur, Kanpur 208016, India*

Published[2] in *Structural and Multidisciplinary Optimization*, DOI: 10.1007/s00158-014-1091-1
Submitted on 8 March 2013, Revised on 20 March 2014, Accepted on 26 March 2014

Abstract: This paper presents computational shape optimization of adhesive microstructures. Adhesion is described by van der Waals interactions. These are incorporated into a nonlinear, geometrically exact beam formulation. The cross section of the beam is considered to vary along the beam length. The resulting shape variations are then used for optimization, by maximizing the contact surface of the beam, maximizing the external work during peeling, and minimizing the strain energy. A nonlinear finite element formulation is used to discretize and solve the resulting system. Optimization is then based on a genetic algorithm. Apart from the actual optimization procedure, this work also focuses on the problem formulation and the corresponding choice of problem parameters. In order to explore the properties of the design space, a large number of benchmark cases is examined. The optimization parameters of the model are investigated and several design guidelines are drawn. It is shown that, depending on the chosen model parameters, the computed optimal beam shape resembles the shape of gecko spatulae.

Keywords: shape optimization, peeling strips, gecko adhesion, computational contact mechanics, geometrically exact beam theory, nonlinear finite element methods

List of important symbols

A	cross section area
A_s	effective shear area
A_c	contact area
A_H	Hamaker constant for van der Waals adhesion
c_c	weighting factor for contact term in objective function
c_p	weighting factor for peeling term in objective function
E	Young's modulus
G	shear modulus
H	beam height / thickness
H_min	admissible minimum beam height
H_max	admissible maximum beam height
H''_max	maximum for second derivative of H w.r.t. S
I	second moment of area
L	beam length
L_0	unit length used for normalization

[1] Corresponding author, email: sauer@aices.rwth-aachen.de, phone: +49 241 80-99129, fax: +49 241 80-628498

L_c	contact length / length of adhesive part
M_c	contact moment due to van der Waals adhesion
N_total	population size for the genetic algorithm
N_child	number of children per generation
N_new	number of new random geometries per generation
N_mut	number of mutations per generation
ν	Poisson's ratio
P	reaction force due to imposed displacement
Π	potential energy
$\overline{\Pi}$	normalized potential energy
Ψ	objective function
r_0	molecular equilibrium distance of the Lennard-Jones potential
S	beam axis coordinate
$\boldsymbol{T}_\mathrm{c}$	contact traction due to van der Waals adhesion
u	vertical displacement imposed at the left boundary
V	beam volume
V_max	admissible maximum volume
W	beam width
W_min	admissible minimum beam width
W_max	admissible maximum beam width
W''_max	maximum for second derivative of W w.r.t. S

1 Introduction

Thin adhesive films play an essential role for both natural and technical applications: These include the adhesion mechanism of insects and lizards, and the fabrication of bio-inspired adhesives. The knowledge of how the adhesion and detachment behavior of peeling strips can be modified, facilitates designing artificial materials with strongly adhesive surfaces. This motivates us investigating how the adhesion properties of a thin strip can be improved by optimizing its shape.

The geometry-dependent peeling behavior of adhesive microstructures has been subject of various studies: Autumn et al. (2002) have stated that the strength of adhesion of gecko setae[3] is strongly influenced by their surface geometry. An analytical approach has been considered in order to maximize the peeling force of cylindrical adhesive fibrils (Gao et al., 2005; Gao and Yao, 2004). Subsequently, Yao and Gao (2006) have developed a more general model for the optimal shape of two adhering elastic surfaces. Additional studies propose both scaling guidelines for different shapes of fibril tips (Spolenak et al., 2005b), and "adhesion design maps" (Spolenak et al., 2005a; Greiner et al., 2009); those maps relate the desired contact strength to geometrical and material properties. Nevertheless, analytical models are restricted to simple geometric shapes; they further cannot account for large deformations during peeling.

Apart from analytical studies, the dependence of the adhesion strength on the fibril geometry has been investigated in various experimental (Gorb et al., 2007; del Campo et al., 2007; Greiner et al., 2007), theoretical (Carbone et al., 2011), as well as in numerical studies (Peng et al., 2010; Pantano et al., 2011; Zhang et al., 2011; Carbone and Pierro, 2012; Peng and Chen, 2012; Afferrante and Carbone, 2012). The latter, however, do not account for shape optimization by means of an optimization method.

[3] Gecko toes are covered with smooth hairs (*setae*) that split up into fine tips (*spatulae*).

Using topology optimization, Sylves et al. (2009) have designed thin adhesives that show a desired force-displacement relation during peeling. This study includes both the delamination of beams and of thin plates. Nevertheless, since the proposed method is limited to to geometrically linear problems, this approach is not applicable to large deformations as they may occur for thin adhesive fibrils.

The shape design of beams has been investigated by Gams et al. (2010), considering flexible and dynamic frame structures under large rotations. The study discusses a gradient-based approach to determine the optimal width and thickness of a load-moving robot arm. The structure is modeled by using a geometrically exact beam theory; the model therefore accounts for large deformations. Nevertheless, the work of Gams et al. (2010) is neither related to adhesion-dominated nor to general contact problems.

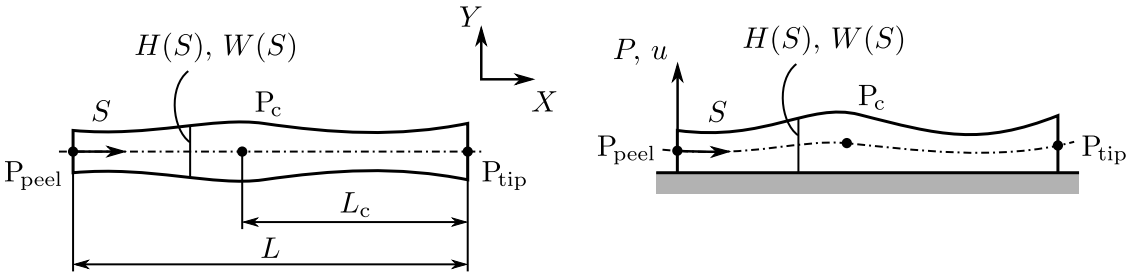

(a) Beam geometry (b) Initial configuration

Figure 1: Setup of the thin adhesive strip; the peeling force is applied at the left boundary

Our aim is to design the shape of flexible peeling strips undergoing large displacements and rotations. For this purpose, we investigate how a thin strip should be shaped in order to (1) adhere strongly to the substrate, and (2) minimize large strains, which can cause either material damage or plastic deformation. In the present study, we consider a strip with an elongated, beam-like structure. Its rectangular cross section varies in both the height, $H(S)$, and width, $W(S)$, along the beam axis, $S \in [0, L]$ (Fig. 1(a)). In the initial configuration, the lower strip surface is fully attached to a planar, rigid substrate (Fig. 1(b)); the beam axis is thus initially curved.[4] In the interval between the points $\mathrm{P_c}$ and $\mathrm{P_{tip}}$ ($S \in [L-L_c, L]$), the strip is adhering to the substrate by van der Waals forces. The left boundary of the strip is pulled upward by prescribing a vertical displacement at the point $\mathrm{P_{peel}}$.

The modeling and computation of the detachment process is done with the 2D finite beam element formulation of Sauer and Mergel (2014) for thin film peeling. This formulation is based on the geometrically nonlinear beam theory of Reissner (1972). Our study is motivated by the understanding of shape optimization of adhesive strips. In this preliminary investigation, we focus on identifying and discussing both objectives and additionally required constraints. For optimization, we use a genetic (stochastic) algorithm; this facilitates exploring the non-convex design space discussed here. Importantly, the large deformation analysis considered for the peel-off computation may not converge for various intermediate designs. For those cases, gradient computation may not be possible, which would make classical, gradient-based optimization approaches stall. Considering a stochastic method, we can circumvent such cases by artificially penalizing any non-convergent designs. We intend to reformulate the design problem, facilitating the use of gradient-based approaches, in the future.

The remaining sections of this paper are structured as follows: Section 2 first summarizes the

[4]Note that the strip geometry is generated by using a straight beam axis, see Fig. 1(a).

beam model equations and defines the considered optimization problem. The governing equations are then discretized within a finite element framework. Section 3 discusses the applied optimization method. In Section 4, the peeling behavior of differently shaped benchmark geometries is studied. The presented optimization method is used to study optimal shapes for different criteria and constraints. Section 5 finally concludes this paper.

2 Model equations

In this section, we present the continuum mechanical equations that are used to model the peeling of a thin strip from a flat rigid substrate. Afterwards, we discuss suitable optimization criteria and provide additional constraints on the strip geometry. We then summarize the discretized equations that are used to solve the problem numerically.

2.1 Mechanical equations

The peeling strip that we are considering here has a thin and elongated geometry. We thus model it as a beam, using the beam adhesion formulation of Sauer and Mergel (2014). This model is based on the geometrically exact beam theory of Reissner (1972), see also Wriggers (2008). According to this theory, the beam's cross sections remain planar, but not necessarily perpendicular to the axis. It can thus account for finite strain, bending, and shearing within the beam. In the following, we consider the full detachment process as quasi-static. The external work provided to peel the strip from the substrate is either transformed into internal energy or into the contact energy that is required to separate the two bodies (Sauer, 2011). The incremental form of the work balance is thus given by

$$\mathrm{d}\Pi_{\mathrm{ext}} = \mathrm{d}\Pi_{\mathrm{int}} + \mathrm{d}\Pi_{\mathrm{c}}. \tag{1}$$

As depicted in Fig. 1(b), the strip is lifted by the vertical displacement, u, prescribed at the left boundary, $\mathrm{P}_{\mathrm{peel}}$; this results in a reaction force, P. Thereby, the externally applied energy changes by

$$\mathrm{d}\Pi_{\mathrm{ext}} = P(u)\ \mathrm{d}u. \tag{2}$$

Considering linear elastic material behavior, the internally stored energy is given by

$$\mathrm{d}\Pi_{\mathrm{int}} = \int_L \mathrm{d}\boldsymbol{\varepsilon}^{\mathrm{T}}\, \boldsymbol{D}\, \boldsymbol{\varepsilon}\ \mathrm{d}S, \tag{3}$$

where the vector $\boldsymbol{\varepsilon}$ is composed of the axial, shear, and bending strains (Sauer and Mergel, 2014). The material tensor, $\boldsymbol{D} = \mathrm{diag}\big(EA, GA_{\mathrm{s}}, EI\big)$, contains Young's modulus, E, and the shear modulus, G. Considering a rectangular strip cross section, the area, A, the shear area, A_{s}, and the second moment of area, I, are obtained by $A = H\,W$, $A_{\mathrm{s}} = 5/6\,A$, and $I = 1/12\,H^3\,W$ (Sauer and Mergel, 2014).

For a beam, the total contact energy can be stated as (Sauer and Mergel, 2014)

$$\mathrm{d}\Pi_{\mathrm{c}} = -\int_{L_{\mathrm{c}}} \mathrm{d}\boldsymbol{d}^{\mathrm{T}} \begin{bmatrix} \boldsymbol{T}_{\mathrm{c}} \\ M_{\mathrm{c}} \end{bmatrix} \mathrm{d}S, \tag{4}$$

where the vector $\boldsymbol{d}$ contains the $X-$ and $Y-$displacements of the beam axis as well as the rotation, ψ, of the cross section. The distributed contact force, $\boldsymbol{T}_{\mathrm{c}}$, and contact moment, M_{c}, are modeled by using the body force formulation of Sauer and Mergel (2014). Since the

considered peeling direction is perpendicular to the substrate, any tangential forces (e.g. due to friction) would hardly affect the peeling behavior of the strip; this has been investigated by Sauer and Holl (2013) and Sauer and Mergel (2014). We therefore consider contact between the strip and the substrate as frictionless.

For the sake of simplicity, we assume that the beam thickness, H, is small compared to the bending radius during film peeling. In this case, the contact moment is negligible (Sauer, 2011); $M_\mathrm{c} \approx 0$.[5] For van der Waals interaction, the contact line force, $\boldsymbol{T}_\mathrm{c}$ can be determined by (Sauer and Mergel, 2014),

$$\boldsymbol{T}_\mathrm{c} = \frac{T(r_1)}{\cos\psi}\,\boldsymbol{n}_\mathrm{s}, \qquad T(r) = \frac{A_\mathrm{H}\,W}{2\pi r_0^3}\left[\frac{1}{45}\left(\frac{r_0}{r}\right)^9 - \frac{1}{3}\left(\frac{r_0}{r}\right)^3\right], \tag{5}$$

where $\boldsymbol{n}_\mathrm{s}$ is the normal vector of the substrate, and r_1 is the distance between the lower strip surface and the substrate.[6] The term $T(r)$ is obtained by considering the Lennard-Jones potential, which is discussed e.g. in the book by Israelachvili (2011). Here, A_H is the Hamaker constant (Israelachvili, 2011), and r_0 is the molecular equilibrium distance of the potential.

2.2 Shape optimization

Regarding the requirement of strong adhesion, (1) the contact energy and (2) the externally applied work – both measured for full separation – are appropriate objectives for maximization. Those are

$$\Pi_\mathrm{ext}^\infty = \Pi_\mathrm{ext}(u_\infty), \qquad \Pi_\mathrm{c}^\infty = w_\mathrm{adh}^\infty\, A_\mathrm{c}, \tag{6}$$

where u_∞ is the displacement for full detachment, A_c is the total contact area, and w_adh^∞ is the work of adhesion for full separation (Sauer, 2011),

$$A_\mathrm{c} = \int_{L_\mathrm{c}} W \,\mathrm{d}S, \qquad w_\mathrm{adh}^\infty = \sqrt[3]{15}\,\frac{A_\mathrm{H}}{16\pi r_0^2}. \tag{7}$$

Further, the minimization of the internal energy at detachment is suitable to prevent large strains. If we reconsider the balance of work (1), we can observe a dependence of the three energy terms. We do not know, however, when the beam deforms most strongly during detachment. For this reason, we consider the maximum of the internal energy during the detachment process,

$$\Pi_\mathrm{int}^\mathrm{max} = \max_{u\in[0,u_\infty]} \Pi_\mathrm{int}. \tag{8}$$

Our objective function Ψ that is minimized thus consists of three different terms, which can be weighted by two parameters. We arrive at the following problem statement:

Problem statement

Find $H(S)$ and $W(S)$ such that

$$\Psi = \frac{c_\mathrm{p}}{\overline{\Pi}_\mathrm{ext}^\infty} + \overline{\Pi}_\mathrm{int}^\mathrm{max} + \frac{c_\mathrm{c}}{\overline{\Pi}_\mathrm{c}^\infty} \tag{9}$$

is minimized subject to the constraints discussed in Section 2.3.

[5] The error caused by this simplification is supposed to be negligible to those that arise from the model assumption of thin and elongated structures.

[6] Eq. (5) holds if H is larger than a few nanometers (Sauer, 2011; Sauer and Mergel, 2014).

Here, the quantities $\overline{\Pi}_\bullet$ denote the normalized[7] expressions of the total peeling energy, $\Pi_{\text{ext}}^{\infty}$, the peak internal energy, $\Pi_{\text{int}}^{\max}$, (also denoted as deformation energy), and the total contact energy, Π_{c}^{∞}. The factors $c_{\text{p}}, c_{\text{c}} \geq 0$ are introduced to weight the different criteria.

Although the optimized quantities in Eq. (9) are physically justified, the problem can be stated differently by choosing alternative objectives. One could, for instance, minimize only the strain, $||\boldsymbol{\varepsilon}||$, instead of the peak internal energy. Note that since the weightings c_{p} and c_{c} are constants here, Eq. (9) is a single-objective problem. Nevertheless, regarding further studies following this preliminary investigation, the consideration of multi-objective problems will be promising.

2.3 Design constraints

The peeling strip problem (9) has to fulfill additional conditions, which are specified in the following:

(i) Beam volume

The strip must not exceed the maximum volume, $V_{\max}$,

$$V \leq V_{\max}, \qquad V = \int_L H\, W \, \mathrm{d}S. \tag{10}$$

(ii) Box constraint

The height and width must lie within prescribed intervals. This condition is also referred to as box constraint, see e.g. Christensen and Klarbring (2009),

$$H(S) \in [H_{\min}, H_{\max}], \qquad W(S) \in [W_{\min}, W_{\max}], \qquad S \in [0, L]. \tag{11}$$

When choosing the interval limits, we are aware that the height, width, and volume are correlated.[8]

(iii) Second derivatives of height and width

Since the film surface should be sufficiently smooth, we restrict the second derivatives of H and W w.r.t. S,

$$|H''(S)| \leq H''_{\max}, \qquad |W''(S)| \leq W''_{\max}, \qquad S \in [0, L]. \tag{12}$$

(iv) Quasi-static behavior

The strip must satisfy the quasi-static equilibrium condition (1) during peeling.

Note that constraints (i) – (iii), concerning the beam geometry itself, can be enforced *a priori* without peeling simulation. Constraint (iv) involves the computation of the peeling process; therefore, it must be verified *a posteriori*.

[7] We use $1/\left(EL_0^3\right)$ for normalization here, where E is Young's modulus and L_0 is a unit length.

[8] To ensure that the geometry can admit the limits, condition $H_{\min}W_{\min} \leq V_{\max}/L \leq H_{\max}W_{\max}$ must be fulfilled.

2.4 Numerical description

The equations discussed in the previous section are now discretized within a finite element (FE) framework. This procedure is only outlined here; we refer to (Sauer and Mergel, 2014) for a more detailed description. To enhance both accuracy and efficiency, we consider independent meshes for (1) the optimization problem (indicated with superscript 'opt'), and (2) the solution of the discretized FE beam equations (indicated with 'h'). We use in both meshes linear shape functions, which are denoted in the following as $\mathbf{N}_e^{\text{opt}} = \mathbf{N}_e^h = \mathbf{N}_e$.[9] The mesh elements have a constant length, respectively L^h and L^{opt}, where L^{opt} is a multiple of L^h (Fig. 2).

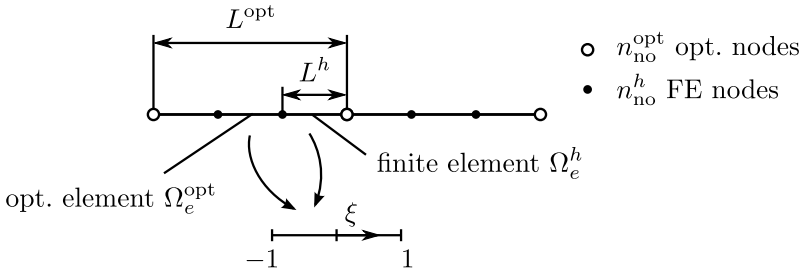

Figure 2: Interpolation of the finite element and optimization meshes; for integration, the element domains are mapped onto the reference domain, $\xi \in [-1, 1]$

The cross-sectional properties, $\left(H_e^h, W_e^h\right)$ for finite element Ω_e^h and $\left(H_e^{\text{opt}}, W_e^{\text{opt}}\right)$ for optimization element Ω_e^{opt}, are then approximated by

$$H_e^\bullet = \mathbf{N}_e\, \mathbf{H}_e^\bullet \qquad \text{and} \qquad W_e^\bullet = \mathbf{N}_e\, \mathbf{W}_e^\bullet, \qquad \bullet = h,\, \text{opt}, \tag{13}$$

where $\mathbf{H}_e^\bullet$ and $\mathbf{W}_e^\bullet$ are the nodal quantities of element $\Omega_e^\bullet$, $e = 1, \ldots, n_{\text{el}}^\bullet$.

2.4.1 FE equilibrium equation

During peeling, the beam must fulfill the FE equilibrium equation

$$\mathbf{f}_{\text{int}}^h + \mathbf{f}_{\text{c}}^h - \mathbf{f}_{\text{ext}}^h = \mathbf{0}, \tag{14}$$

where both the internal force, $\mathbf{f}_{\text{int}}^h$, and the contact force, $\mathbf{f}_{\text{c}}^h$, are specified in (Sauer and Mergel, 2014). We enforce strip peeling by applying a Dirichlet boundary condition; at each load step, the displacement of the left boundary, u^h, increases by the constant value, Δu. Eq. (14) is linearized using Newton's method.

2.4.2 Discretized optimization problem

The discretized form of the optimization problem (9) is stated as:

$$\min_{H_I^{\text{opt}},\, W_I^{\text{opt}}} \quad \Psi^h \quad \text{subject to} \quad \text{the constraints in Sect. 2.4.3}, \tag{15}$$

where Ψ^h is given by

$$\Psi^h = \frac{c_{\text{p}}}{\left(\overline{\Pi}_{\text{ext}}^{\infty}\right)^h} + \left(\overline{\Pi}_{\text{int}}^{\max}\right)^h + \frac{c_{\text{c}}}{\left(\overline{\Pi}_{\text{c}}^{\infty}\right)^h}. \tag{16}$$

[9] The shape function $\mathbf{N}_e$ is evaluated in the reference domain, $\xi \in [-1, 1]$, by $\mathbf{N}_e(\xi) = [(1-\xi)/2, (1+\xi)/2]$.

Here, H_I^{opt} and W_I^{opt} respectively denote the height and width of node $I = 1, \ldots, n_{\mathrm{no}}^{\mathrm{opt}}$. The discretized peeling energy, $(\Pi_{\mathrm{ext}}^{\infty})^h$, is computed by integrating Eq. (2). For the remaining two quantities, we find

$$(\Pi_{\mathrm{int}}^{\max})^h = \max_{u^h} (\Pi_{\mathrm{int}})^h, \qquad (\Pi_{\mathrm{int}})^h = \sum_{e=1}^{n_{\mathrm{el}}^h} \left[\frac{1}{2} \int_{L_e} \boldsymbol{\varepsilon}_e^{\mathrm{T}} \, \boldsymbol{D}^h \, \boldsymbol{\varepsilon}_e \, \mathrm{d}S \right] \tag{17}$$

and

$$(\Pi_{\mathrm{c}}^{\infty})^h = w_{\mathrm{adh}}^{\infty} \cdot \sum_{e=1}^{n_{\mathrm{ce}}^h} \left[\int_{L_e} W^h \, \mathrm{d}S \right], \tag{18}$$

where n_{ce}^h is the number of finite elements discretizing the adhesive part, $S \in [L - L_{\mathrm{c}}, L]$.

2.4.3 Discretized optimization constraints

The discretized optimization constraints show a form very similar to the continuum equations in Section 2.3:

(i) Beam volume

$$V^{\mathrm{opt}} \leq V_{\max}, \qquad V^{\mathrm{opt}} = \sum_{e=1}^{n_{\mathrm{el}}^{\mathrm{opt}}} \left[\int_{L_e} H^{\mathrm{opt}} \, W^{\mathrm{opt}} \, \mathrm{d}S \right]. \tag{19}$$

(ii) Box constraint

$$H_I^{\mathrm{opt}} \in [H_{\min}, H_{\max}], \qquad W_I^{\mathrm{opt}} \in [W_{\min}, W_{\max}], \qquad I = 1, \ldots, n_{\mathrm{no}}^{\mathrm{opt}}. \tag{20}$$

(iii) Second derivatives of height and width

$$\frac{\left| F_{I+1}^{\mathrm{opt}} - 2\, F_I^{\mathrm{opt}} + F_{I-1}^{\mathrm{opt}} \right|}{\left(L^{\mathrm{opt}} \right)^2} \leq F''_{\max}, \qquad F = H, W, \qquad I = 2, \ldots, n_{\mathrm{no}}^{\mathrm{opt}} - 1. \tag{21}$$

(iv) Quasi-static behavior

Static equilibrium (14) must be fulfilled at each load step.

3 Optimization method

This section discusses the optimization method applied in the present study. Within this work, we predominantly focus on the problem formulation instead of the optimization procedure itself, which justifies the application of a stochastic optimization method. In the present case, we consider a genetic algorithm (GA). With a stochastic approach like the GA, we can conveniently eliminate non-convergent strip designs by penalizing structures that do not fulfill the quasi-static peeling behavior.

Tab. 1 shows the schematic of the algorithm implemented here. First, an initial population is generated; this population must fulfill constraints (i) – (iii) from Section 2.4.3. For each generation, the best-ranked geometries are combined into child geometries; these geometries

may slightly mutate from their parents. In addition, a small percentage of each generation can mutate itself. The worst-rated geometries are eliminated and replaced by randomly generated geometries.

In the following, the objective function, Ψ, is also referred to as cost function. We further consider the design variables of the beam (i.e. the nodal values for the height and width) as a genetic string with a certain cost, Ψ. The algorithm is tested for validation on a trivial

Initial population $(i = 1, \ldots, N_{\text{total}})$

1. generate valid geometry (Appx. A.1)
2. perform peeling computation
3. compute cost according to Eq. (16)

Generation loop

1. sort geometries according to their cost
2. eliminate the $N_{\text{child}}+N_{\text{new}}+N_{\text{mut}}$ worst-rated geometries
3. arrange N_{child} best-rated geometries to random pairs, generate from each pair two children (Appx. A.2)
4. obtain mutations of the N_{mut} best-rated geometries (Appx. A.3) (original geometries are still in population)
5. generate N_{new} valid geometries (Appx. A.1)
6. perform peeling computation for $N_{\text{child}}+N_{\text{new}}+N_{\text{mut}}$ new geometries
7. compute cost for $N_{\text{child}}+N_{\text{new}}+N_{\text{mut}}$ geometries according to Eq. (16)
8. check if N_{mut} mutations show smaller costs than original geometries, set cost of worse-rated to a large value in order to discard them

Table 1: Schematic of the implemented genetic algorithm (GA)

optimization problem,

$$\min_x \Psi, \qquad \Psi = \left(1 - \tfrac{1}{2}\cos 2x\right)\left(x^2 + 1\right), \qquad x \in [-15, 15], \tag{22}$$

where Ψ is a non-convex function showing multiple minima. For this test problem, the best genetic string approximates the absolute minimum, $\Psi(0) = 0.5$, very fast: For the optimization parameters given in Tab. 11, the relative error of the exact solution and the smallest cost of the 10^{th} generation is less than 10^{-6}. Nevertheless, while it is generally believed that the absolute minimum can be determined when using a genetic algorithm, the latter may require numerous function evaluations to converge to it. In other words, convergence to an absolute minimum within a specified number of generations cannot be guaranteed.

In principle, genetic algorithms can be used to detect multiple local minima. Depending on how those minima differ in their cost, however, genetic strings that have obtained a local minimum are replaced soon by those approaching a minimum with smaller cost.

4 Results

Before applying the optimization method discussed in Section 3 to problem (15), we perform a feasibility study in order to analyze the influence of differently curved strip heights and widths. Afterwards, we present peeling film shapes that we obtain with the genetic algorithm for differently weighted optimization criteria. We then investigate several geometry parameters.

4.1 Benchmark cases

This section demonstrates the spectrum of feasible beam shapes by studying several test geometries. For these shapes, both the energy terms of Eq. (16) and the maximum peeling force are studied.

4.1.1 Shape generation

In order to obtain 25 differently shaped strips, we consider the following five curves respectively for the height, H, and width, W:

$$F_{\mathrm{I}}(S) = c_F - d_F \cdot \cos\left(\pi\, S/L\right) \cdot 0.5\, L, \tag{23}$$
$$F_{\mathrm{II}}(S) = c_F + d_F \cdot (S - 0.5\, L), \tag{24}$$
$$F_{\mathrm{III}}(S) = c_F, \tag{25}$$
$$F_{\mathrm{IV}}(S) = c_F - d_F \cdot (S - 0.5\, L), \tag{26}$$
$$F_{\mathrm{V}}(S) = c_F + d_F \cdot \cos\left(\pi\, S/L\right) \cdot 0.5\, L. \tag{27}$$

The resulting shapes are sketched in Fig. 3. The curve parameters, c_F, $d_F > 0$, are chosen such that all geometries have (1) equal volume, V, and (2) a lower surface with area, A_{low}[10]; see Tab. 9. The remaining geometry, material, and adhesion parameters are given in Tab. 10. The peeling, deformation, and contact energies, $\Pi_{\mathrm{ext}}^{\mathrm{ref}}$, $\Pi_{\mathrm{int}}^{\mathrm{ref}}$, and $\Pi_{\mathrm{c}}^{\mathrm{ref}}$, obtained for $(H_{\mathrm{III}}, W_{\mathrm{III}})$, are used in the following sections for normalization.[11]

4.1.2 Influence on the peeling force

We investigate the influence of the strip height and width separately by comparing the most characteristic shapes: H_{I}, H_{III}, and H_{V} combined with W_{III}; and vice versa. This results in five different shapes, which are marked in green in Fig. 3. The corresponding peeling reaction forces are shown in Fig. 4. It can be seen in Fig. 4(a) that for a constant height, an increasing width towards $\mathrm{P}_{\mathrm{tip}}$ increases both the maximum peeling force, $P_{\max}$, and the displacement for full separation, u_∞. This observation agrees well with the results of Pantano et al. (2011). Nevertheless, for the test cases considered here, $P_{\max}$ also increases for those shapes that become thicker towards $\mathrm{P}_{\mathrm{tip}}$; this contradicts the observations made by Pantano et al. (2011). We thus assume that the relation of the force and the strip height is nonlinear; this issue is further investigated in a following study; see (Mergel and Sauer, 2014).

Fig. 5(a) outlines the spectrum of peeling reaction forces that are obtained for the benchmark shapes. Here, the shapes $(H_{\mathrm{I}}, W_{\mathrm{I}})$, $(H_{\mathrm{I}}, W_{\mathrm{V}})$, $(H_{\mathrm{V}}, W_{\mathrm{I}})$, and $(H_{\mathrm{V}}, W_{\mathrm{V}})$ (i.e. the geometries in the corners of Fig. 3) are considered. The smallest and largest maximum forces occur respectively

[10] The lower surface area is given by $A_{\mathrm{low}} = \int_L W \, \mathrm{d}S$.
[11] These terms are given by $\Pi_{\mathrm{ext}}^{\mathrm{ref}} = 297.267\, EL_0^3$, $\Pi_{\mathrm{int}}^{\mathrm{ref}} = 127.587\, EL_0^3$, and $\Pi_{\mathrm{c}}^{\mathrm{ref}} = 229.950\, EL_0^3$.

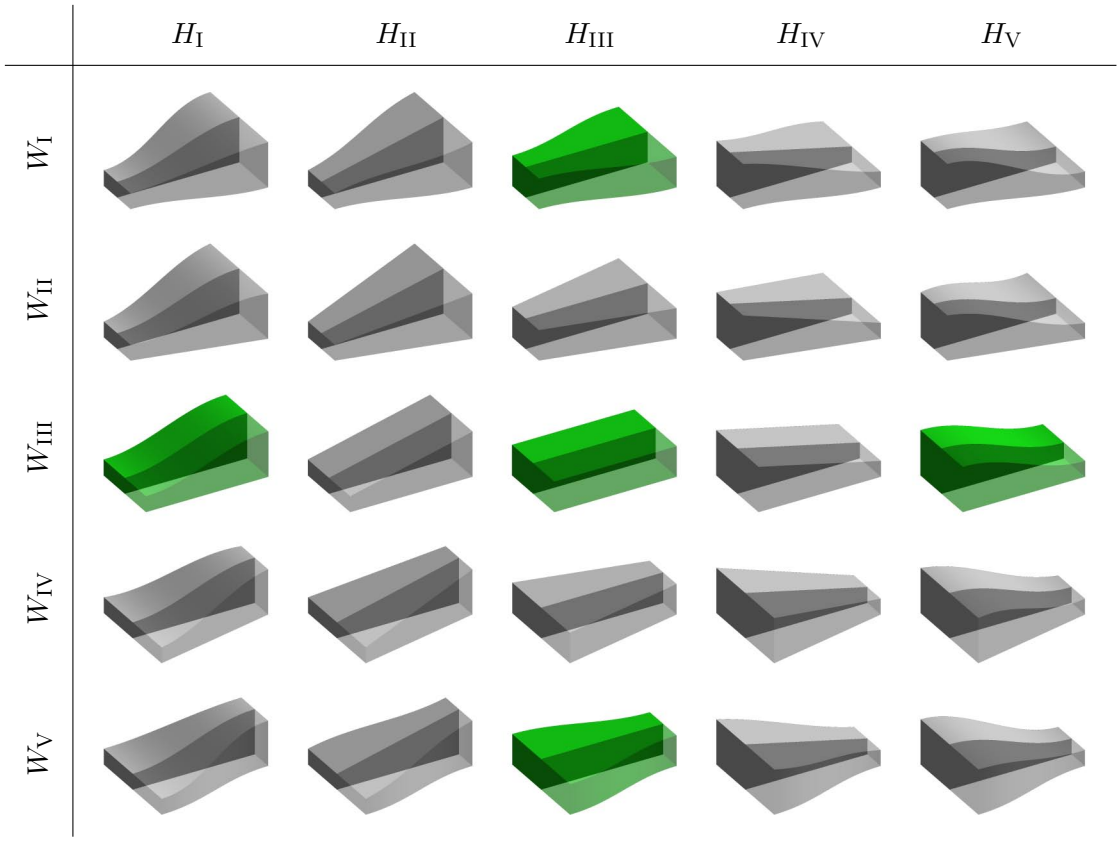

Figure 3: Schematic representation of the 25 benchmark geometries; the peeling force is applied at the left boundary, $\mathrm{P_{peel}}$; the right boundary is denoted as $\mathrm{P_{tip}}$ (shapes are exaggerated for better visualization)

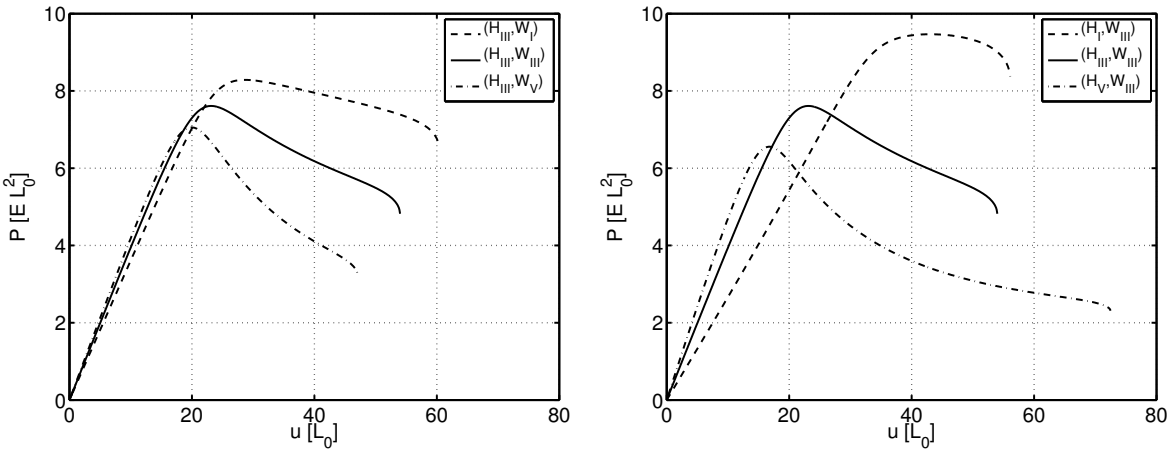

(a) Constant height, H_{III} (green column in Fig. 3)

(b) Constant width, W_{III} (green row in Fig. 3)

Figure 4: Peeling force for the benchmark geometries marked in green in Fig. 3

for (H_V, W_V) (bottom right) and (H_I, W_I) (top left). This agrees well with the observations made before. It is apparent from geometry (H_I, W_V) that a large maximum reaction force does not necessarily imply a high detachment stability. It is not desirable, however, to design a strip that resists large peeling forces but fully detaches for small imposed displacements.[12] This observation motivates us not considering the peak force but rather maximizing the total externally applied work.

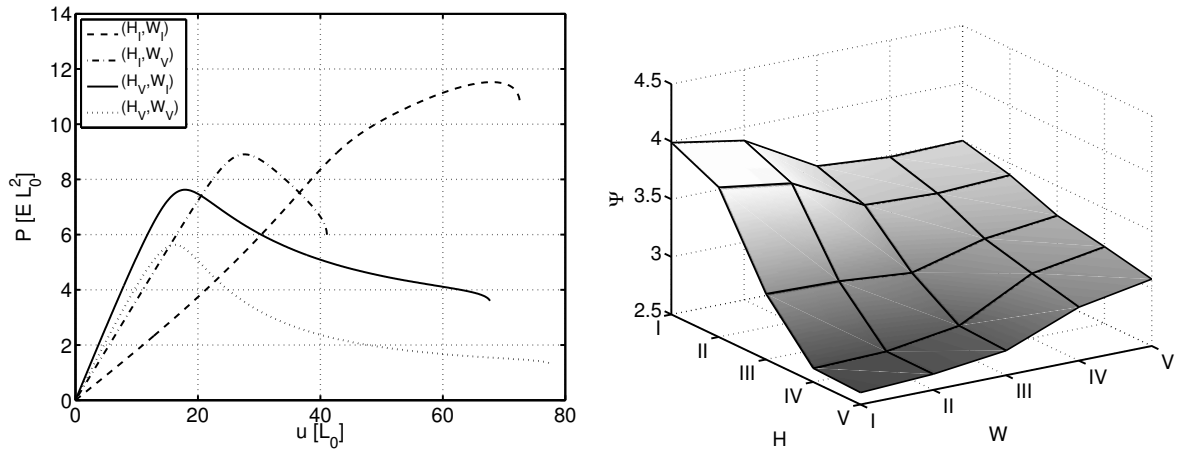

(a) Force for the strips shown in the corners of Fig. 3

(b) Evaluated cost for $c_p = c_c = 1$

Figure 5: Peeling force, P, and cost, Ψ, for the benchmark geometries considering the weighting parameters $c_p = c_c = 1$

4.1.3 Influence on the energy terms

Tab. 2 shows the three energy terms from Eq. (16) for all benchmark cases. The characteristic shapes that are highlighted in Fig. 3 are marked in bold. The total contact energy, Π_c^∞, is independent of the strip height; it increases with the contact area, A_c, which is largest for W_I, and smallest for W_V. In analogy to the external forces, both the applied work, Π_{ext}^∞, and the deformation energy, Π_{int}^{max}, increase if the film becomes either wider or thicker towards the boundary P_{tip}. Inversely, both quantities decrease if the height and width become smaller in this direction. The total contact energy, Π_c^∞, and the external work, Π_{ext}^∞, seem to be correlated to each other, see Tab. 2. The observation coincides with the assumption that the strain energy becomes largest right before full separation, which would yield with Eq. (1): $\Pi_{ext}^\infty \approx \Pi_{int}^{max} + \Pi_c^\infty$. This issue is further discussed in Section 4.3.

4.1.4 Influence on the cost function

Fig. 5(b) and Tab. 2 show the cost, Ψ, obtained for all benchmark geometries with the weighting parameters $c_p = c_c = 1$. One finds that for these weightings, the optimal geometry has a large contact area and becomes thinner at its attached tip; this can be seen for (H_V, W_I) and (H_{IV}, W_I) in the top right corner of Fig. 3. Both structures show – in comparison to the rectangular strip, (H_{III}, W_{III}) – larger peeling energies but smaller deformation energies. Considering adhesion mechanisms in nature, we observe that these two geometries roughly correspond to the shape of a gecko spatula tip (Fig. 6(a)).

[12] This would be the case for very stiff structures.

	(H, W)	Ψ	$\overline{\Pi}_{\text{ext}}^{\infty}$	$\overline{\Pi}_{\text{int}}^{\text{max}}$	$\overline{\Pi}_{\text{c}}^{\infty}$
1.	$(H_{\text{V}}, W_{\text{I}})$	2.604	1.141	0.902	1.212
2.	$(H_{\text{IV}}, W_{\text{I}})$	2.620	1.110	0.894	1.212
3.	$(H_{\text{V}}, W_{\text{II}})$	2.637	1.106	0.875	1.167
4.	$(H_{\text{IV}}, W_{\text{II}})$	2.639	1.074	0.851	1.167
5.	$\boldsymbol{(H_{\text{V}}, W_{\text{III}})}$	**2.714**	**0.916**	**0.623**	**1.000**
6.	$(H_{\text{IV}}, W_{\text{III}})$	2.735	0.889	0.610	1.000
7.	$(H_{\text{V}}, W_{\text{IV}})$	2.964	0.731	0.397	0.833
8.	$\boldsymbol{(H_{\text{III}}, W_{\text{III}})}$	**3.000**	**1.000**	**1.000**	**1.000**
9.	$(H_{\text{III}}, W_{\text{II}})$	3.054	1.246	1.394	1.167
10.	$(H_{\text{IV}}, W_{\text{IV}})$	3.062	0.712	0.457	0.833
11.	$\boldsymbol{(H_{\text{III}}, W_{\text{I}})}$	**3.071**	**1.296**	**1.474**	**1.212**
12.	$(H_{\text{V}}, W_{\text{V}})$	3.081	0.697	0.377	0.788
13.	$(H_{\text{IV}}, W_{\text{V}})$	3.167	0.676	0.420	0.788
14.	$(H_{\text{III}}, W_{\text{IV}})$	3.168	0.773	0.675	0.833
15.	$\boldsymbol{(H_{\text{III}}, W_{\text{V}})}$	**3.242**	**0.729**	**0.602**	**0.788**
16.	$(H_{\text{II}}, W_{\text{IV}})$	3.367	0.867	1.013	0.833
17.	$(H_{\text{II}}, W_{\text{III}})$	3.393	1.179	1.545	1.000
18.	$(H_{\text{II}}, W_{\text{V}})$	3.398	0.804	0.886	0.788
19.	$(H_{\text{I}}, W_{\text{IV}})$	3.487	0.888	1.160	0.833
20.	$(H_{\text{I}}, W_{\text{V}})$	3.502	0.815	1.006	0.788
21.	$\boldsymbol{(H_{\text{I}}, W_{\text{III}})}$	**3.535**	**1.220**	**1.715**	**1.000**
22.	$(H_{\text{II}}, W_{\text{II}})$	3.709	1.541	2.203	1.167
23.	$(H_{\text{II}}, W_{\text{I}})$	3.800	1.623	2.358	1.212
24.	$(H_{\text{I}}, W_{\text{II}})$	3.883	1.594	2.399	1.167
25.	$(H_{\text{I}}, W_{\text{I}})$	3.992	1.682	2.573	1.212

Table 2: Cost function terms for the benchmark geometries using $c_{\text{p}} = c_{\text{c}} = 1$; the shapes that are highlighted in green in Fig. 3 are marked in bold

4.2 Peeling strip design using a genetic algorithm

After studying the influence of different shapes on our optimization criteria, we use the genetic algorithm from Section 3 to optimize both the strip height and width w.r.t. problem (15).

4.2.1 Optimal shape

First, we choose the weighting parameters $c_{\text{p}} = c_{\text{c}} = 1$. Additional parameters (which are also used in the following sections) can be found in Tab. 11. The best-rated shape of the 400^{th} generation is shown in Fig. 6(b) – 6(d).[13] The geometry is very similar to the shape of a gecko spatula; cf. Fig. 6(a) and 6(b). Regarding the benchmark test, the strip resembles closest the best-rated geometry, $(H_{\text{V}}, W_{\text{I}})$. Note that for the optimized geometry, the inclinations of both the height and width are small at the boundaries; this may be caused by the procedure used for the geometry generation (Tab. 6). Fig. 7(a) shows the strip deformation for four different configurations. Fig. 7(b) compares the peeling force to the force observed for the shape $(H_{\text{V}}, W_{\text{I}})$. Initially, the peeling forces agree well for both shapes. Both the maximum

[13] The beam axis is initially curved (Fig. 1). The strip, however, is only insignificantly shorter than L when considering Cartesian coordinates, (X, Y); e.g. $X(L) = 0.994\, L$ for the shape in Fig. 6.

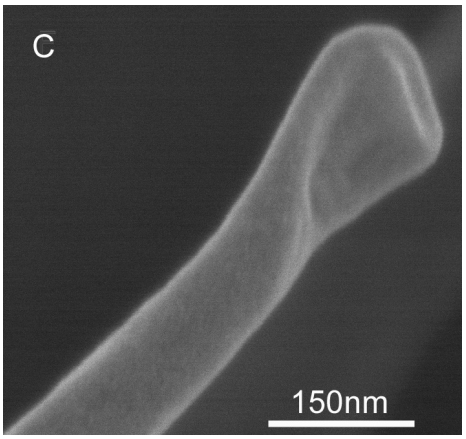

(a) Electron microscopy of a gecko spatula, adopted with permission from J. R. Soc. Interface (Rizzo et al., 2006)

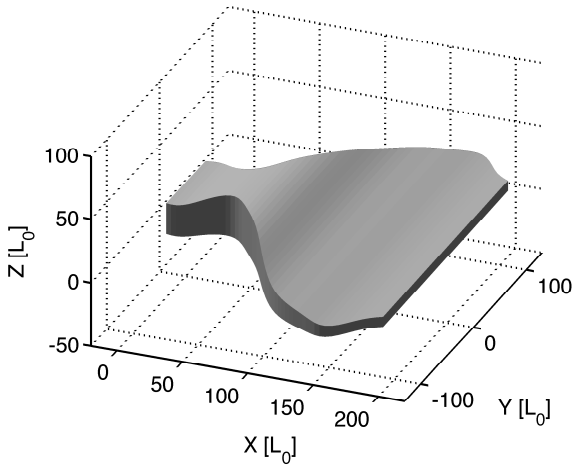

(b) 3D view

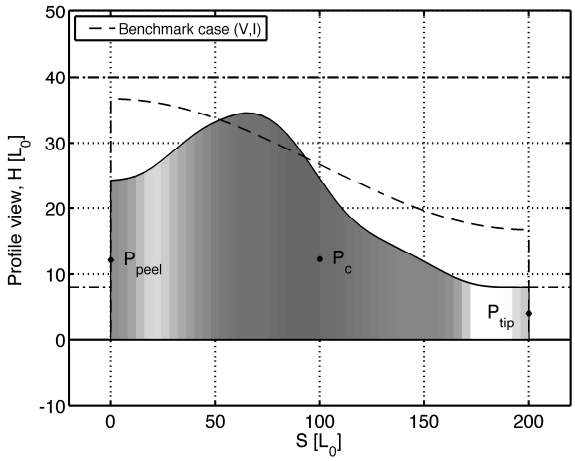

(c) Height (distorted profile view)

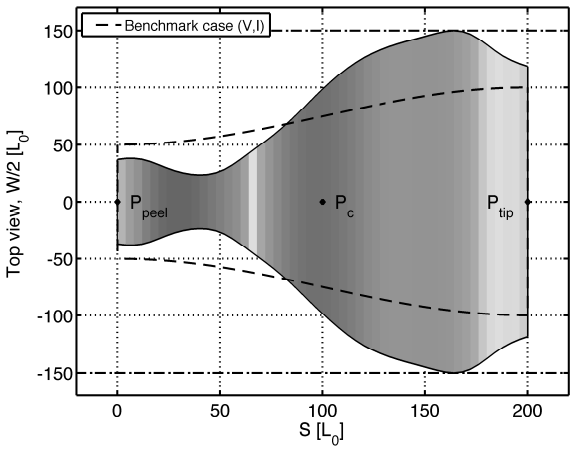

(d) Width (distorted top view)

Figure 6: Comparison of the shape of a gecko spatula and the best geometry obtained for $c_\mathrm{p} = c_\mathrm{c} = 1$ (GA, 400 generations)

force and the corresponding displacement are very similar; the good agreement is probably caused by similar cross sections at $\mathrm{P_c}$.

We recognize that the shapes obtained with the genetic algorithm are comparable to the best-rated benchmark cases. This verifies our implemented optimization method. We further observe that the detachment stability of the optimized shape, indicated by u_∞, is nearly twice as large as for shape $(H_\mathrm{V}, W_\mathrm{I})$. The externally applied work therefore increases from $1.141\,\Pi_\mathrm{ext}^\mathrm{ref}$ to $1.569\,\Pi_\mathrm{ext}^\mathrm{ref}$. In addition, the optimized structure is deformed less while having a larger contact area; thus, the cost is remarkably smaller: $\Psi = 1.948$ compared to $\Psi = 2.604$ for the benchmark case.

The minimum cost of the population decreases significantly in the first 60 generations of the genetic algorithm, but hardly improves afterwards. It remains constant for the last 130 generations, which may imply convergence to the optimal solution. Nevertheless, using a stochastic algorithm, one cannot guarantee that the obtained solution is the absolute minimum. As ex-

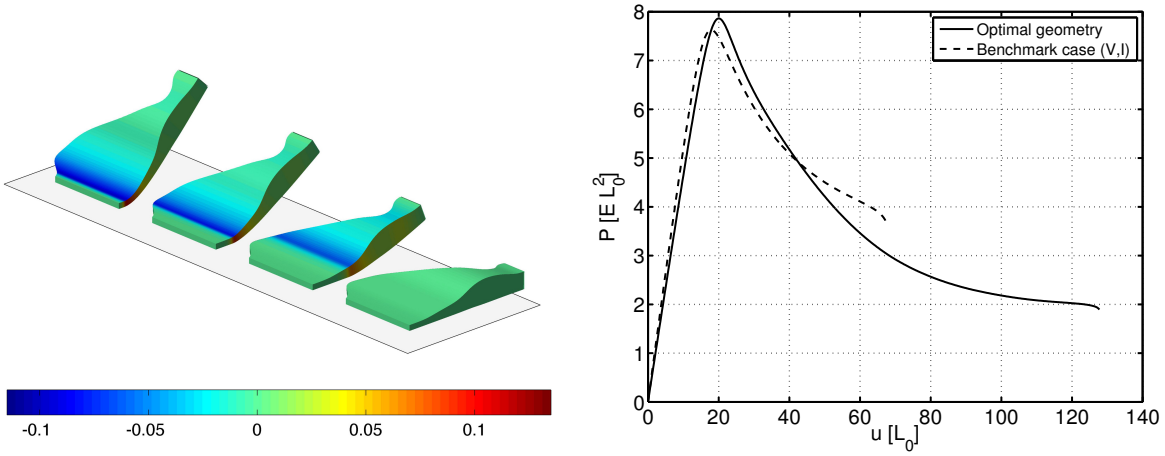

(a) Deformation for $u/L_0 = 0$, 40, 80, 120

(b) Peeling force

Figure 7: Deformation and peeling force of the geometry obtained for $c_\mathrm{p} = c_\mathrm{c} = 1$ (GA, 400 generations)

pected, Ψ converges for a fixed geometry if both the load increment, Δu, and the number of finite elements, n_el^h, are refined.

4.2.2 Extension of the optimization space

We now extend the design space by refining the optimization mesh from 50 to 100 elements; $n_\mathrm{el}^\mathrm{opt} = 100$. Fig. 8 compares the shape obtained after 1600 generations to the original geometry from Section 4.2.1. The cost, $\Psi = 1.946$, of the new structure is slightly smaller than $\Psi = 1.948$ for $n_\mathrm{el}^\mathrm{opt} = 50$; the strip shapes, however, differ remarkably. The extended optimization space must include the original space; therefore, Ψ does not increase with a finer optimization mesh. In addition, extending the design space, it is very likely to obtain a minimum that is smaller than the previous one; this can be observed for the present case.

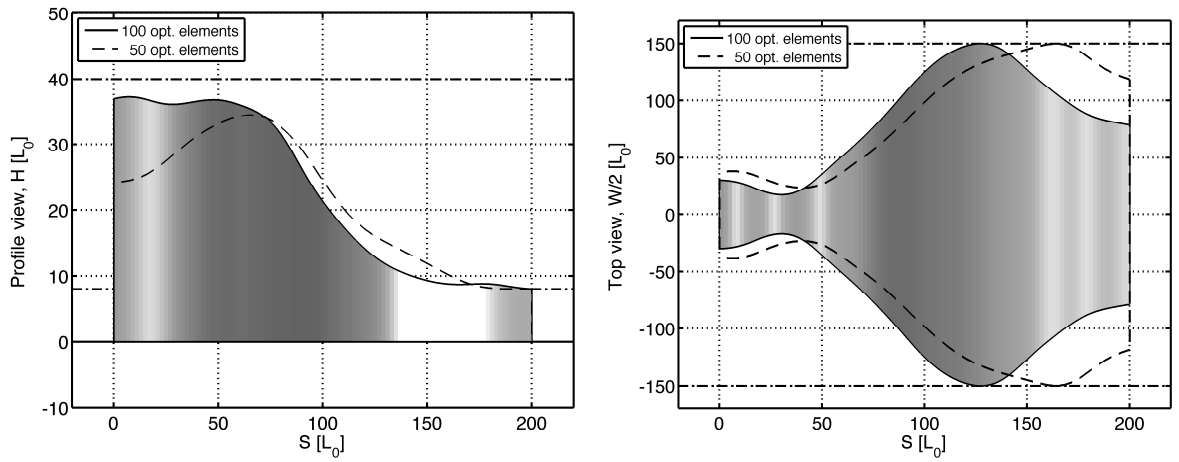

(a) Height (distorted profile view)

(b) Width (distorted top view)

Figure 8: Best-rated shape obtained for 100 optimization elements (GA, 1600 generations) in comparison to results for 50 elements (GA, 400 generations; see Section 4.2.1)

4.3 Variation of the weighting parameters

The results of the previous sections have been obtained with constant weightings, $c_\mathrm{p} = c_\mathrm{c} = 1$. This section presents optimal strip shapes for varying weighting parameters. In order to study the spectrum of feasible geometries, we vary both parameters strongly; here, we choose c_p, $c_\mathrm{c} = 1/10$, 1, 10, which leads to 9 different test cases. Fig. 9 depicts the best geometries obtained after 400 generations of the genetic algorithm. The geometry in the middle corresponds to the solution that is discussed in Section 4.2.

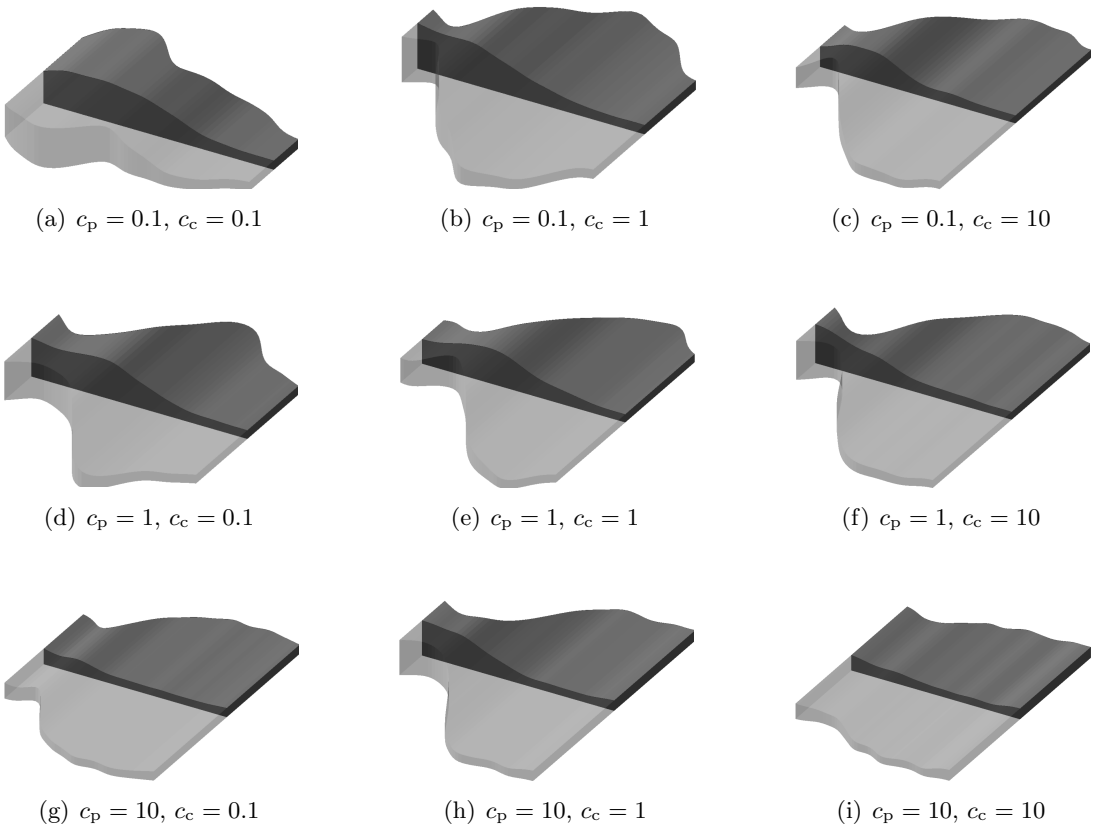

(a) $c_\mathrm{p} = 0.1$, $c_\mathrm{c} = 0.1$ (b) $c_\mathrm{p} = 0.1$, $c_\mathrm{c} = 1$ (c) $c_\mathrm{p} = 0.1$, $c_\mathrm{c} = 10$

(d) $c_\mathrm{p} = 1$, $c_\mathrm{c} = 0.1$ (e) $c_\mathrm{p} = 1$, $c_\mathrm{c} = 1$ (f) $c_\mathrm{p} = 1$, $c_\mathrm{c} = 10$

(g) $c_\mathrm{p} = 10$, $c_\mathrm{c} = 0.1$ (h) $c_\mathrm{p} = 10$, $c_\mathrm{c} = 1$ (i) $c_\mathrm{p} = 10$, $c_\mathrm{c} = 10$

Figure 9: Best-rated beam shapes varying the weighting parameters, c_p and c_c (GA, 400 generations); the peeling force is applied at the left boundary

Tab. 3 shows both the volume and the energy terms of the best-rated shapes. Note that the magnitudes of the cost, Ψ, cannot be compared, because they depend on c_p and c_c. The most significant geometries occur for $c_\mathrm{p} = c_\mathrm{c} = 0.1$ and $c_\mathrm{p} = c_\mathrm{c} = 10$, where the strain energy is weighted most and least strongly. For the other parameter combinations, the strip tends to increase in width and decrease in thickness. Regardless of the weightings, the beam volume tends to increase to the maximum permitted value. This suggests that we should additionally minimize the beam volume.

As Fig. 9 shows, the shape of the strip is similar if the parameters, c_p and c_c, are switched. Even for $c_\mathrm{p} = 0.1$, $c_\mathrm{c} = 10$ and $c_\mathrm{p} = 10$, $c_\mathrm{c} = 0.1$ – where both parameters change by the factor 100 – differences can be observed only at the left tip. In addition, Tab. 3 indicates that the externally applied work increases with the weighting for the contact energy, and vice versa. This observation agrees with the results in Section 4.1.3. We can conclude that, regarding those

c_p	c_c	$V \,/\, V_\mathrm{max}$	$\overline{\Pi}^{\infty}_{\mathrm{ext}}$	$\overline{\Pi}^{\mathrm{max}}_{\mathrm{int}}$	$\overline{\Pi}^{\infty}_{\mathrm{c}}$
0.1	0.1	0.999	0.623	0.244	0.722
0.1	1	1.000	1.346	0.585	1.528
0.1	10	0.991	1.777	1.081	1.921
1	0.1	0.999	1.297	0.586	1.462
1	1	1.000	1.569	0.746	1.772
1	10	0.879	1.814	1.113	1.942
10	0.1	0.804	1.900	1.250	1.954
10	1	0.893	1.980	1.474	1.954
10	10	0.975	2.066	1.734	1.960

Table 3: Peeling, deformation, and contact energy for the best-rated shapes varying the weighting parameters c_p and c_c (GA, 400 generations)

three terms, it would be sufficient to maximize either the external work or the contact area. Consequently, only one weighting parameter would be required here.

4.4 Variation of the maximum volume

The considered design space depends on the geometry parameters that are chosen for the constraints of Section 2.3. Here, we give an exemplary study of their influence, investigating only the maximum volume, V_max, here. Denoting the maximum value from Section 4.2 as V^0_max $\left(V^0_\mathrm{max} = 6 \cdot 10^5 \, L_0^3\right)$, we vary the volume by $V_\mathrm{max} \,/\, V^0_\mathrm{max} = 2/3,\ 1,\ 3/2$. As Fig. 10 shows, the

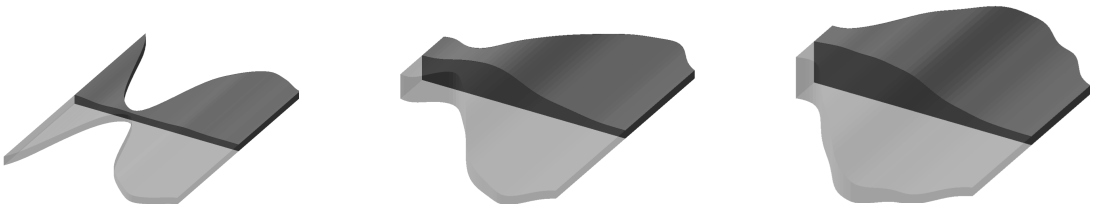

(a) $V_\mathrm{max} = 2/3 \; V^0_\mathrm{max}$ (b) $V_\mathrm{max} = 1 \, V^0_\mathrm{max}$ (c) $V_\mathrm{max} = 3/2 \, V^0_\mathrm{max}$

Figure 10: Best-rated beam shapes varying the maximum volume, V_max (GA, 400 generations); the peeling force is applied at the left boundary

maximum permitted volume influences the optimal beam shape strongly. For all parameters considered here, the structure flattens to a thin strip at P_tip. The maximum height increases with increasing V_max. Since the minimum width is chosen very small ($W_\mathrm{min} = 5 \, L_0$), the peeling strip may become very slim. We note that large variations in the cross section are not properly captured by a beam theory. Tab. 4 compares both the volume and the energy terms measured for the three shapes. For $V_\mathrm{max} = 2/3 \, V^0_\mathrm{max}$, the peeling strip does not attain the maximum volume. Although this strip is very thin, it shows the largest strain energy; this is probably caused by the large gradient in the strip width. Thus, a study of the derivative, $\partial W / \partial S$, could be of interest.

$V_{\max} \,/\, V_{\max}^0$	$V \,/\, V_{\max}$	$\overline{\Pi}_{\text{ext}}^{\infty}$	$\overline{\Pi}_{\text{int}}^{\max}$	$\overline{\Pi}_{\text{c}}^{\infty}$	Ψ
2/3	0.818	1.620	0.924	1.771	2.106
1	1.000	1.569	0.746	1.772	1.948
3/2	0.999	1.498	0.584	1.735	1.828

Table 4: Peeling, deformation, and contact energy for the best-rated shapes varying the maximum volume, $V_{\max}$ (GA, 400 generations)

4.5 Variation of the contact length

Finally, we study the influence of the contact length by varying $L_{\text{c}} \,/\, L = 0.25, 0.5, 0.75$ for $c_{\text{p}} = c_{\text{c}} = 1$. Fig. 11 shows the shapes that are obtained with the genetic algorithm for different contact lengths. Note that $L_{\text{c}} = 0.5\, L$ corresponds to the test case of Section 4.2. We observe

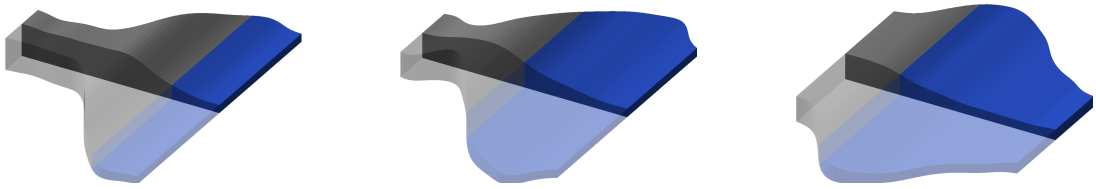

(a) $L_{\text{c}} = 0.25\, L$ (b) $L_{\text{c}} = 0.5\, L$ (c) $L_{\text{c}} = 0.75\, L$

Figure 11: Best-rated beam shapes varying the contact length, L_{c} (GA, 400 generations); the peeling force is applied at the left boundary; the adhesive part of the strip is marked in blue

that the adhesive part of the strip approaches the minimum thickness, $H_{\min}$. The non-adhesive part, which is peeled off first, tends to be a thick beam with small width. At the transition between the two parts (P_{c} in Fig. 1), the width tends to adopt the maximum value, $W_{\max}$.

Fig. 12 shows the forces required to peel the strips of Fig. 11 from the substrate. The longer the adhesive part, the larger are (1) the maximum force and (2) the displacement for full detachment, u_{∞}: If the contact length is increased by $0.25\, L$, the peak force almost doubles. For increasing L_{c}, both the externally applied work and the contact energy increase, while the strain energy decreases (Tab. 5); thus, the cost, Ψ, improves regardless of the weightings, c_{p} and c_{c}.

$L_{\text{c}} \,/\, L$	$V \,/\, V_{\max}$	$\overline{\Pi}_{\text{ext}}^{\infty}$	$\overline{\Pi}_{\text{int}}^{\max}$	$\overline{\Pi}_{\text{c}}^{\infty}$	Ψ
0.25	1.000	0.955	0.771	0.939	2.884
0.50	1.000	1.569	0.746	1.772	1.948
0.75	0.999	1.941	0.609	2.216	1.575

Table 5: Peeling, deformation, and contact energy of the best-rated shapes varying the contact length, L_{c} (GA, 400 generations)

In the present study, we restrict ourselves to a constant strip length, L. In order to investigate the optimal length of adhesive microstructures, other parameters apart from the ratio $L_{\text{c}} \,/\, L$ have to be studied. In particular, the peeling behavior can also depend on the strip length, L, compared to the range of adhesion, r_0.

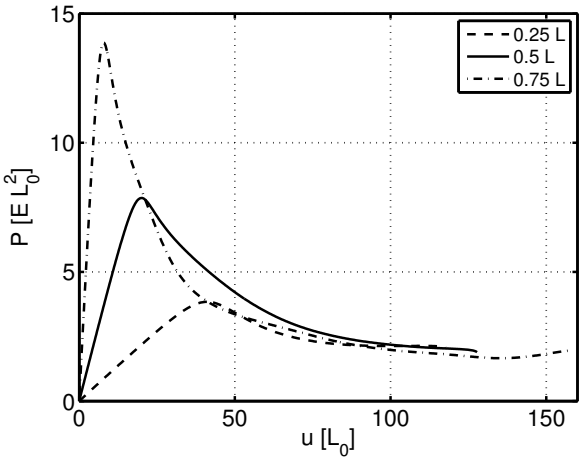

Figure 12: Peeling force for the best-rated beam shape varying the contact length, L_c (GA, 400 generations)

5 Conclusion

We present a novel shape design study for flexible adhesive microstructures undergoing finite deformations during peeling. This study includes both the application of an optimization method and the peeling analysis using a nonlinear beam finite element model. Our aim is to determine – as a preliminary investigation – objectives and constraints that are important for the shape design of thin adhesive strips. To get a first impression of optimum shapes for various criteria, we apply a genetic algorithm here.

We aim to obtain a flexible and elongated peeling strip that adhere to the substrate strongly. These requirements can be achieved by

1. the maximization of the externally applied work,
2. the maximization of the total contact area, and
3. the minimization of the strain energy.

The three quantities are studied by considering various benchmark shapes. We observe that, if the strip increases towards the attached tip in width, both the maximum required peeling force and the external work increase significantly. Further, we assume that (1) the relation between the strip height and the peeling force is nonlinear, and (2) also the derivatives of the height and width w.r.t. the beam axis are important. By performing a parameter study, we determine model parameters that provide strip geometries very similar to a gecko spatula. Compared to a rectangular strip, those structures increase the external peeling work, but decrease the strain energy.

The underlying design problem is investigated for various parameters and differently weighted objectives. For a further investigation, the consideration of multi-criteria optimization will be promising. In addition, since stochastic methods like the genetic algorithm are inefficient compared to gradient-based approaches, the problem will be reformulated in order to facilitate the application of gradient-based approaches.

Apart from the shape, the adhesion of microstructures is influenced by several other factors. Recently, Peisker et al. (2013) have investigated setae of the ladybird beetle; they provide the

evidence that the adhesive fibrils have a varying material stiffness. Since the authors conclude in their study that this can increase adhesion, it would be interesting to consider both the shape and the material properties in the design process.

In addition, the applied contact model can be modified to account for stiction; this allows us varying the direction of peeling. Since several adhesion mechanisms are anisotropic[14], the peeling direction may also influence the optimum shape of microstructures. This is under further investigation by the authors (Mergel and Sauer, 2014). Additionally, the objectives in the presented design approach can be combined with self-cleaning or non-clumping properties. A long-term aim is the extension of the presented model to adhesive structures with arbitrary shaped surface.

A Genetic algorithm

This section contains supplemental information on the genetic algorithm applied here. In the following, the nodal height, H_I^{opt}, and width, W_I^{opt}, are abbreviated by F_I.

A.1 Geometry generation

New random geometries are generated according to the algorithm outlined in Tab. 6. The initially obtained curves are quite uneven; they are thus smoothed by a filter, considering a hat-shaped filter function with a constant width. We note that this procedure restricts our optimization space. The influence of the filter width should therefore be objective of a further study.

Omitting the volume constraint (19), we observe that the nodal values of the obtained geometries are equally distributed along the intervals $[H_{\min}, H_{\max}]$ and $[W_{\min}, W_{\max}]$. Depending on the maximum permitted volume, $V_{\max}$, however, the random geometries approach $H_{\max}$ and $W_{\max}$ less frequently than smaller values.

Iteration until volume constraint (19) is fulfilled

1. generate nodal height and width, F_I, $I = 1, \ldots, n_{\text{no}}^{\text{opt}}$
   - i. generate first value, F_1, fulfilling box constraint (20)
   - ii. continue with $I = 2, \ldots, n_{\text{no}}^{\text{opt}}$
     - compute upper/lower boundary for F_I, F_A and F_B, fulfilling the box and slope constraints (20) & (21)
     - obtain new value, $F_I = F_A + (F_B - F_A)\,\phi_I, \quad \phi_I \in [0, 1]$
2. apply a smoothing filter to F_I, $I = 1, \ldots, n_{\text{no}}^{\text{opt}}$

Table 6: Geometry generation for the genetic algorithm

[14] This has been discussed for gecko adhesion e.g. by Autumn et al. (2000) and Autumn et al. (2006).

A.2 Generation of child geometries

The height and width, $\left(H_I^{\mathrm{p}}, W_I^{\mathrm{p}}\right)$ and $(H_I^{\mathrm{m}}, W_I^{\mathrm{m}})$, of two parent geometries are combined to obtain two child geometries; this procedure is described in Tab. 7. The quantities μ_{abs}, $\mu_{\mathrm{rel}} \ll 1$ denote relative and absolute mutation rates.

Iteration until box, slope, and volume constraints (19) – (21) are fulfilled

generate nodal height and width, $F_I,\ I = 1, \ldots, n_{\mathrm{no}}^{\mathrm{opt}}$

1. generate random values $\phi_A^{\mathrm{abs}}, \phi_B^{\mathrm{abs}} \in [1-\mu_{\mathrm{abs}}, 1+\mu_{\mathrm{abs}}]$ and $\phi_A^{\mathrm{rel}}, \phi_B^{\mathrm{rel}} \in [-\mu_{\mathrm{rel}}, 1+\mu_{\mathrm{rel}}]$
2. obtain two nodal random numbers, $\quad I = 1, \ldots, n_{\mathrm{no}}^{\mathrm{opt}}$
$$\phi_I^{\mathrm{abs}} = \phi_A^{\mathrm{abs}} + \left(\phi_B^{\mathrm{abs}} - \phi_A^{\mathrm{abs}}\right) \cdot (I-1) / \left(n_{\mathrm{no}}^{\mathrm{opt}} - 1\right),$$
$$\phi_I^{\mathrm{rel}} = \phi_A^{\mathrm{rel}} + \left(\phi_B^{\mathrm{rel}} - \phi_A^{\mathrm{rel}}\right) \cdot (I-1) / \left(n_{\mathrm{no}}^{\mathrm{opt}} - 1\right)$$
3. combine values F_I^{p} and F_I^{m} to
$$F_I = \phi_I^{\mathrm{abs}} \left[\phi_I^{\mathrm{rel}} \cdot F_I^{\mathrm{p}} + \left(1 - \phi_I^{\mathrm{rel}}\right) \cdot F_I^{\mathrm{m}}\right], \quad I = 1, \ldots, n_{\mathrm{no}}^{\mathrm{opt}}$$

Table 7: Generation of child geometries for the genetic algorithm

A.3 Mutation

The best-rated geometries of each generation are mutated by a relative mutation rate, $\mu \ll 1$. This procedure is illustrated in Tab. 8.

Iteration until box, slope, and volume constraints (19) – (21) are fulfilled

generate nodal height and width, $F_I,\ I = 1, \ldots, n_{\mathrm{no}}^{\mathrm{opt}}$

1. generate random values $\phi_A, \phi_B \in [1-\mu, 1+\mu]$
2. mutate original geometry, F_I^{old}, by
$$F_I = \phi_I \cdot F_I^{\mathrm{old}}, \quad I = 1, \ldots, n_{\mathrm{no}}^{\mathrm{opt}}$$

Table 8: Mutation of the best geometries for the genetic algorithm

B Parameters

The following section summarizes the parameters used for the test cases in Section 4.

B.1 Curve parameters for the benchmark case

The following parameters are identical for all benchmark strips: $c_W = 150\,L_0$, $d_W = 0.5$, and $d_H = 0.1$. The parameter c_H, indicating the thickness of the strip at $S = L/2$, is adjusted s.t. the strips have both an identical volume, V, and a lower surface with area, A_{low}; see Tab. 9.

	$c_H\ [L_0]$ for $H_{\text{I}} - H_{\text{V}}$				
	H_{I}	H_{II}	H_{III}	H_{IV}	H_{V}
$W = W_{\text{I}}$	23.3402	23.6518	25	26.3482	26.6598
$W = W_{\text{II}}$	23.6518	23.8889	25	26.1111	26.3482
$W = W_{\text{III}}$	25	25	25	25	25
$W = W_{\text{IV}}$	26.3482	26.1111	25	23.8889	23.6518
$W = W_{\text{V}}$	26.6598	26.3482	25	23.6518	23.3402

Table 9: Curve parameter c_H for the benchmark geometries of Section 4.1; the remaining parameters are $d_H = 0.1$, $c_W = 150\,L_0$, and $d_W = 0.5$

geometry	$L_0 = 1\,\text{nm}, \quad L = 200\,L_0, \quad V = 7.5 \cdot 10^5\,L_0^3, \quad A_{\text{low}} = 3 \cdot 10^4\,L_0^2$
material	$E = 2\,\text{GPa}, \quad \nu = 0.2$
adhesion	$A_{\text{H}} = 10^{-19}\,\text{J}, \quad r_0 = 0.4\,\text{nm}, \quad L_{\text{c}} = 0.5\,L$

Table 10: Geometry, material, and adhesion parameters for the benchmark case in Section 4.1

B.2 Parameters for the genetic algorithm

Tab. 11 summarizes the parameters used in Sections 4.2 – 4.5.

geometry	$L_0 = 1\,\text{nm}, \quad L = 200\,L_0, \quad V_{\max} = 6 \cdot 10^5\,L_0^3,$ $H_{\min} = 8\,L_0, \quad H_{\max} = 40\,L_0, \quad W_{\min} = 5\,L_0, \quad W_{\max} = 300\,L_0,$ $H''_{\max} = 1/(16\,L_0), \quad W''_{\max} = 7/(16\,L_0)$
material	$E = 2\,\text{GPa}, \quad \nu = 0.2$
adhesion	$A_{\text{H}} = 10^{-19}\,\text{J}, \quad r_0 = 0.4\,\text{nm}, \quad L_{\text{c}} = 0.5\,L$
computation	$n_{\text{el}}^{\text{opt}} = 50, \quad n_{\text{el}}^{h} = 4\,n_{\text{el}}^{\text{opt}}$
optimization	$N_{\text{total}} = 100, \quad N_{\text{child}} = 20, \quad N_{\text{new}} = 36, \quad N_{\text{mut}} = 4,$ $\mu_{\text{abs}} = 0.05, \quad \mu_{\text{rel}} = 0.25, \quad \mu = 0.01, \quad 400$ generations

Table 11: Parameters for the genetic algorithm used in Sections 4.2 – 4.5

Acknowledgements

The authors are grateful to the Alexander von Humboldt foundation supporting A. Saxena, and to the German Research Foundation (grants SA1822/5-1 and GSC111) supporting J. C. Mergel and R. A. Sauer.

References

Afferrante, L. and Carbone, G. (2012). Biomimetic surfaces with controlled direction-dependent adhesion. *J. R. Soc. Interface*, **9**:3359–3365.

Autumn, K., Dittmore, A., Santos, D., Spenko, M., and Cutkosky, M. (2006). Frictional adhesion: A new angle on gecko attachment. *J. Exp. Biol.*, **209**:3569–3579.

Autumn, K., Liang, Y. A., Hsieh, S. T., Zesch, W., Chan, W. P., Kenny, T. W., Fearing, R., and Full, R. J. (2000). Adhesive force of a single gecko foot-hair. *Nature*, **405**:681–685.

Autumn, K., Sitti, M., Liang, Y. A., Peattie, A. M., Hansen, W. R., Sponberg, S., Kenny, T. W., Fearing, R., Israelachvili, J. N., and Full, R. J. (2002). Evidence for van der Waals adhesion in gecko setae. *Proc. Natl. Acad. Sci. U.S.A.*, **99**(19):12252–12256.

Carbone, G. and Pierro, E. (2012). Sticky bio-inspired micropillars: Finding the best shape. *Small*, **8**(9):1449–1454.

Carbone, G., Pierro, E., and Gorb, S. N. (2011). Origin of the superior adhesive performance of mushroom-shaped microstructured surfaces. *Soft Matter*, **7**(12):5545–5552.

Christensen, P. W. and Klarbring, A. (2009). *An Introduction to Structural Optimization*, volume 153 of *Solid Mechanics and its Applications*. Springer.

del Campo, A., Greiner, C., and Arzt, E. (2007). Contact shape controls adhesion of bioinspired fibrillar surfaces. *Langmuir*, **23**:10235–10243.

Gams, M., Saje, M., Planinc, I., and Kegl, M. (2010). Optimal size, shape, and control design in dynamics of planar frame structures under large displacements and rotations. *Eng. Optim.*, **42**(1):69–86.

Gao, H., Wang, X., Yao, H., Gorb, S., and Arzt, E. (2005). Mechanics of hierarchical adhesion structures of geckos. *Mech. Mater.*, **37**:275–285.

Gao, H. and Yao, H. (2004). Shape insensitive optimal adhesion of nanoscale fibrillar structures. *Proc. Natl. Acad. Sci. U.S.A.*, **101**(21):7851–7856.

Gorb, S., Varenberg, M., Peressadko, A., and Tuma, J. (2007). Biomimetic mushroom-shaped fibrillar adhesive microstructure. *J. R. Soc. Interface*, **4**:271–275.

Greiner, C., del Campo, A., and Arzt, E. (2007). Adhesion of bioinspired micropatterned surfaces: Effects of pillar radius, aspect ratio, and preload. *Langmuir*, **23**:3495–3502.

Greiner, C., Spolenak, R., and Arzt, E. (2009). Adhesion design maps for fibrillar adhesives: The effect of shape. *Acta Biomater.*, **5**:597–606.

Israelachvili, J. N. (2011). *Intermolecular and Surface Forces*. Academic Press, 3rd edition.

Mergel, J. C. and Sauer, R. A. (2014). On the optimum shape of thin adhesive strips for various peeling directions. *J. Adhesion*, **90**(5-6):526–544.

Pantano, A., Pugno, N. M., and Gorb, S. N. (2011). Numerical simulations demonstrate that the double tapering of the spatulae of lizards and insects maximize both detachment resistance and stability. *Int. J. Fract.*, **171**:169–175.

Peisker, H., Michels, J., and Gorb, S. N. (2013). Evidence for a material gradient in the adhesive tarsal setae of the ladybird beetle *Coccinella septempunctata*. *Nat. Commun.*, **4**. DOI: 10.1038/ncomms2576.

Peng, Z. and Chen, S. (2012). The effect on geometry on the adhesive behavior of bio-inspired fibrils. *Soft Matter*, **8**:9864–9869.

Peng, Z. L., Chen, S. H., and Soh, A. K. (2010). Peeling behavior of a bio-inspired nano-film on a substrate. *Int. J. Solids Struct.*, **47**:1952–1960.

Reissner, E. (1972). On one-dimensional finite-strain beam theory: The plane problem. *J. Appl. Math. Phys. (ZAMP)*, **23**:795–804.

Rizzo, N. W., Gardner, K. H., Walls, D. J., Keiper-Hrynko, N. M., Ganzke, T. S., and Hallahan, D. L. (2006). Characterization of the structure and composition of gecko adhesive setae. *J. R. Soc. Interface*, **3**(8):441–451.

Sauer, R. A. (2011). The peeling behavior of thin films with finite bending stiffness and the implications on gecko adhesion. *J. Adhesion*, **87**(7-8):624–643.

Sauer, R. A. and Holl, M. (2013). A detailed 3D finite element analysis of the peeling behaviour of a gecko spatula. *Comput. Methods Biomech. Biomed. Eng.*, **16**(6):577–591.

Sauer, R. A. and Mergel, J. C. (2014). A geometrically exact finite beam element formulation for thin film adhesion and debonding. *Finite Elem. Anal. Des.*, **86**:120–135.

Spolenak, R., Gorb, S., and Arzt, E. (2005a). Adhesion design maps for bio-inspired attachment systems. *Acta Biomater.*, **1**:5–13.

Spolenak, R., Gorb, S., Gao, H., and Arzt, E. (2005b). Effects of contact shape on the scaling of biological attachments. *Proc. R. Soc. A*, **461**:305–319.

Sylves, K., Maute, K., and Dunn, M. L. (2009). Adhesive surface design using topology optimization. *Struct. Multidiscip. Optim.*, **38**:455–468.

Wriggers, P. (2008). *Nonlinear Finite Element Methods*. Springer, Berlin Heidelberg.

Yao, H. and Gao, H. (2006). Optimal shapes for adhesive binding between two elastic bodies. *J. Colloid Interface Sci.*, **298**:564–572.

Zhang, X., Zhang, X., and Wen, S. (2011). Finite element modeling of the nano-scale adhesive contact and the geometry-based pull-off force. *Tribol. Lett.*, **41**:65–72.